J. COMBIN. MATH. COMBIN. COMPUT. 127b (2025) 3011--3032

Journal of Combinatorial Mathematics
and Combinatorial Computing
www.combinatorialpress.com/jcmcc

Combinatorial Press

Artificial Intelligence Based Analysis System for Standard Energy Meter Current Measurement Module

Xingzhi Liu[1,2,✉], Wenbo Yao[1], Juan Tian[1], Yu Su[1]

[1] *State Grid Chongqing Electric Power Company Marketing Service Center, Chongqing, 401123, China*
[2] *School of Electrical Engineering, Chongqing University, Chongqing, 400030, China*

ABSTRACT
This paper proposes to design the power meter based on TMR current sensor, screen the chips that meet the requirements of the power meter, and stipulate the technical specifications and technical parameters of the power meter based on TMR current sensor. Design the system structure of power meter with TMR current sensor including MCU module, storage module, communication module and so on. And design the main and vice system clocks in the single-phase energy meter with TMR current sensor. Analyze the design of signal acquisition module, bias adjustment and temperature compensation module, communication module and circuit protection module in the current monitoring system. According to the characteristics of the TMR sensor, establish the objective function, improve the GWO algorithm, and optimize the design of the multi-stage magnetic ring structure current sensor. The performance parameters of the TMR sensor are analyzed, and the DC current test and AC current test are conducted to verify the performance of the TMR current sensor measurement module. The accuracy, precision and linearity of the current measurement module are tested, and the relative error between the actual current value and the theoretical current value derived from the formulae in the DC current test and the AC current test are controlled within 5% in the TMR current measurement system. The measurement system based on TMR current sensor meets the current measurement requirements.

Keywords: TMR sensor, GWO algorithm, current measurement, magnetic ring structure

1. Introduction

Electricity is an important secondary energy related to national economy and people's livelihood, power generation, transmission, distribution, power facilities together form a complete power system. Among them, the power meter used to measure electric energy as an economic indicator accounting measurement tool, for the supply and demand sides in the fair power transactions laid a solid

✉ Corresponding author.
E-mail address: 18084020531@163.com (X. Liu).
Received 25 February 2024; Revised 10 June 2024; Accepted 05 November 2024; Published Online 16 April 2025.
DOI: 10.61091/jcmcc127b-169

foundation, and the power meter can be accurately measured this issue involves the interests of many people [1-2]. With the continuous upgrading and transformation of power grid technology, China has achieved great results in the construction of smart grid, as an important part of the smart grid, the energy meter plays a key role in the connection between the power grid and the customers, and is widely used in the collection of power information at the user side, serving both the user and the power supply side, which is also in the process of continuous updating [3-6]. Power meter is a kind of precision electric energy measuring apparatus, so in different operating environments, the accuracy and reliability of power meter measurement becomes a key concern for power supply companies and related enterprises.

With the access of new energy sources such as solar energy, photovoltaic power generation and wind energy, the harmonic voltage and harmonic current components in the power supply system have been increasing, which puts forward higher requirements for the accurate measurement of power meters [7-10]. However, there are many reasons affecting the accuracy of the energy meter, which may be caused by poor contact of terminals, overloading and other causes of meter burning faults [11-12]. Battery factors of energy meter batteries that do not meet the production requirements and oxidization of batteries in sustained high humidity environments [13]. Environmental factors of air quality, magnetic field changes [14-15]. Human factors of incorrect wiring of the energy meter, resulting in short circuit of the circuit board or high current when the meter is in use [16]. The energy meter can provide parameters such as voltage, power, and current, and it is by measuring the product of current and voltage that it calculates the consumption of electrical energy, and the energy meter has different operating characteristics in different current ranges [17-18]. Therefore, current measurement as the core module of the power meter, its performance is directly related to the accuracy and normal operation of power meter metering.

In this paper, the advantages of magnetic field sensors in current measurement are presented, TMR current sensors are introduced, and TMR sensors are characterized. It points out the performance evaluation indexes of magnetic characteristics, improves the multi-stage magnetic ring structure using algorithm optimization, determines the variable parameters of the TMR sensor, improves the GWO algorithm, and develops the ACGWO-BP algorithm, which is used for parameter finding of the BP algorithm. Then the non-dominated sorting genetic algorithm (NSGA-II) is used for multi-objective optimization of the multi-stage size structure, and the ACGWO-BP-NSGA-II optimization design framework is built. The overall design of the energy meter hardware is formulated, breaking down the planning of circuits such as MCU control circuits, describing the signal acquisition module, bias adjustment and temperature compensation module, communication module, and circuit protection module, respectively. The performance of the TMR sensor is analyzed to examine the measurement effect based on the TMR current sensor.

2. Current sensor characterization and optimization

2.1. Current Measurement Techniques Based on Magnetic Sensors

The current measurement technique based on magnetic sensors uses magnetic field as an intermediary, by measuring the magnetic field excited by the current and thus deducing the current.

Magnetic field measurement technology has a long history of development and has been widely researched and applied in the fields of space science, geological exploration, industrial inspection and medical diagnosis. The continuous progress of modern physics and material science has led to the discovery of more magnetic-related physical effects, and has also given rise to a wide variety of magnetic field measurement instruments on the market.

Current measurement methods based on magnetic field sensors require the conversion of the magnetic signal generated by the current into an electrical signal. Magnetic sensors, as the key components of the whole chain, should be selected based on the characteristics of the measured magnetic field by considering the factors of measurement range, accuracy, miniaturization, and cost. Among the magnetic field measurement methods, the measurement range of the magnetic method is too high, and the measurement range of the superconducting effect method is too low. The measurement frequency of the electromagnetic induction method is not able to measure both constant and alternating magnetic fields, and the magnetic resonance method is limited by the size and cost of the device, neither of which is very suitable for making current sensors. Therefore, this paper focuses on magnetoresistive sensors.

Magnetoresistive effect refers to the phenomenon that certain metal or semiconductor materials change their resistance value under the action of an applied magnetic field. The emergence of new material structures, anisotropic magnetoresistance (AMR), giant magnetoresistance (GMR) and tunneling magnetoresistance (TMR) have been studied successively. Since then, magnetoresistive components have developed rapidly and continue to crowd the magnetic sensor market.

2.2. TMR current sensors

The magnetoresistance effect is the effect whereby the resistance of a material changes in response to an applied magnetic field, and this effect is known as the ordinary magnetoresistance (OMR) effect. The magnitude of the magnetoresistance ρ_H is proportional to the square of the product of the magnitude of the magnetic field H and the mobility of the object μ, and the positive scale factor is Z. The expression is shown below:

$$\rho_H = \rho_0 (1 + Z(\mu H)^2) \tag{1}$$

where ρ_H is the magnetoresistance at magnetic field strength H and ρ_0 is the magnetoresistance at magnetic field strength 0 ($H = 0$). Then the expression corresponding to the magnetoresistance effect R_{MR} is:

$$R_{MR} = \frac{\Delta\rho}{\rho_0} = Z(\mu H)^2 \times 100\% \tag{2}$$

Comparison of various magnetoresistive effect performance parameters can be seen, TMR effect resistance value change is much larger, can reach several thousand percent or even infinite. While other magnetoresistive effect is generally only a few dozen percent or a few hundred percent. Moreover, the operating frequency of TMR is higher, which can reach more than 1GHz. Other magnetoresistive effects generally work at frequencies between 10kHz and 200kHz. Finally, TMRs have a wider range of applications and can be used in high-performance devices such as hard disk read/write heads, motor position sensors, magnetic random access memory (MRAM), etc., whereas other magnetoresistive effects have a relatively narrow range of applications.

A magnetic tunneling effect transistor is a device that utilizes the TMR effect to achieve current control, and its basic structure consists of a magnetic tunneling junction (MTJ) element and two electrode layers.The MTJ element consists of a pinning layer, a tunneling barrier layer, and a free layer. The pinned layer consists of a ferromagnetic layer and an antiferromagnetic layer, which has a fixed direction of magnetization. The free layer is another ferromagnetic layer whose magnetization direction can be changed by an external magnetic field. The tunneling barrier layer is a non-magnetic insulating layer that allows electrons between the two ferromagnetic layers to pass through only by quantum tunneling effects. The electrode layers are two conductive layers that are in contact with the antiferromagnetic layer and the free layer, respectively, and are used to provide and collect tunneling current. The electrode layers lie on top of an insulating substrate, which is wider than the electrode layers, and over a bottom substrate made of another material.

The MTJ is the basis of the magnetic tunneling effect transistor, and the spin polarizability of the two ferromagnetic layer electrodes in the MTJ is defined as:

$$Q = \frac{N_{\uparrow} - N_{\downarrow}}{N_{\uparrow} + N_{\uparrow}} \tag{3}$$

where $N_{\uparrow}$ and $N_{\downarrow}$ are the density of states of spin-up and spin-down electrons at the Fermi surface of ferromagnetic metals, respectively.

It can be obtained from the Julliere model:

$$R_{TMR} = \frac{\Delta R}{R_A} = \frac{R_A - R_P}{R_A} = \frac{2Q_1Q_2}{1 + Q_1Q_2} \tag{4}$$

$$R_{TMR} = \frac{\Delta R}{R_P} = \frac{R_A - R_p}{R_P} = \frac{2Q_1Q_2}{1 - Q_1Q_2} \tag{5}$$

where R_P, R_A is the tunneling resistance when the magnetization directions of the two ferromagnetic layers are parallel and antiparallel, respectively. Q_1, Q_2 is the spin polarizability of the two ferromagnetic layer electrodes, respectively. Obviously, if both Q_1 and Q_2 are non-zero, there is a TMR effect in the MTJ, and the larger the spin polarization rate of the two ferromagnetic layer electrodes, the higher the resistance value of R_{TMR} is.

2.2.1. Basic modeling of TMR current sensors. The relationship between the magnitude of the current and the magnetic field can be established based on basic sensing principles. Let there be a small current element in an energized straight wire dl whose current strength has a magnitude of I. According to the Biot-Savart law, the magnetic induction generated by this current element is:

$$dB = \frac{\mu_0}{4\pi} \times \frac{Idl \times \hat{r}}{r^2} \tag{6}$$

where μ_0 is the vacuum permeability, generally taken as $\mu_0 = 4\pi \times 10^{-7}$ (H/m). r is the distance from the current element to the current to be measured. $\hat{r}$ is the unit vector from the current element to the calculation point.

Integrating Eq. (6) gives:

$$B = \frac{\mu_0}{4\pi} \int \frac{Idl \times \hat{r}}{r^2} \tag{7}$$

The basic sensing model of a finite-length straight conductor is shown in Fig. 1, for a finite-length straight conductor, take a section of the current element dl, according to the formula (7) can be known that the long straight conductor at the point of P generated by the magnetic field strength of the magnitude of:

$$B_0 = \frac{\mu_0 I_0}{4\pi L}(\sin\varepsilon_2 - \sin\varepsilon_1) \tag{8}$$

where I_0 is the current to be measured. B_0 is the magnitude of the magnetic induction at point P, L is the perpendicular distance from the conductor at a point P outside the conductor. ε_1 and ε_2 represent the respective angle (the positive direction of the two angles are clockwise).

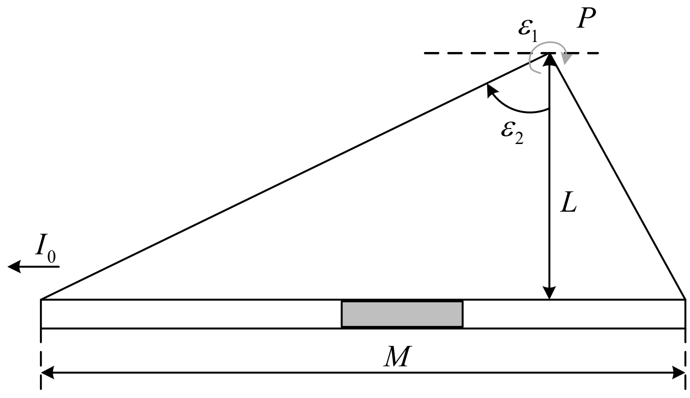

Fig. 1. Basic sensing model of finite length straight conductor

When the energized long straight wire is approximated to be of infinite length, it is easy to know $sin\varepsilon_2 - sin\varepsilon_1 \approx 2$, from which the magnitude of the magnetic induction at point P at this point can be found to be:

$$B_0 = \frac{\mu_0 I_0}{2\pi d} \tag{9}$$

For the TMR current sensor to measure the current, when the conductor to be measured is treated as an infinite length straight conductor, as long as the distance from a point P to the current is known L and the magnetic induction strength of the point, the magnitude of the current to be measured can be found out I_0, which can be calculated from equation (9) as follows:

$$I_0 = \frac{2\pi L}{\mu_0} B_0 \tag{10}$$

In order to further analyze the current formula, the output expression of the TMR chip will be related to the relationship between the current and the magnetic field of an infinitely long straight conductor, which will lead to a finer model of the basic accuracy of the TMR current sensor.

2.2.2. TMR Sensor Characterization. The performance of a TMR sensor is mainly affected by the characteristics of its smallest structural unit, the MTJ [19-20]. The characteristics of the MTJ are mainly temperature characteristics, hysteresis characteristics, and noise characteristics. Among them, the noise of MTJ shows 1/f characteristics in the low frequency band, and the main noise source comes from the electrical and magnetic mechanisms.

1) Temperature Characteristics. The temperature characteristics of TMR components are reflected in the zero drift and sensitivity drift. Due to the preparation of hundreds of MTJ series connection is not fully matched, the presence of spurious parameters caused by the positive and negative half-bridge amplitude response situation there is a difference in the absence of external magnetic field in the environment of the TMR element output is not zero, its value is also changed with the temperature, the phenomenon that is for the zero-point temperature drift. This phenomenon is known as zero point temperature drift. The effect of temperature can be handled to some extent by the Wheatstone bridge structure.

The sensitivity temperature drift refers to the change in the electron spin polarization of the ferromagnetic layer of the magnetic tunnel junction MTJ when the temperature changes, which correspondingly changes the tunneling current on the perpendicular film surface. The effect due to temperature can be somewhat handled by the Wheatstone bridge structure. The sensitivity temperature drift means that when the temperature changes, the electron spin polarization rate of the ferromagnetic layer of the magnetic tunnel junction MTJ changes, which correspondingly changes the tunneling current on the surface of the vertical film.

2) Hysteresis properties. In the category of magnetic materials, it is generally accepted that an ideal ferromagnetic material will have no anisotropy, no interaction between magnetic domains. The magnetization process is reversible back and forth, the magnetic induction B is a single-valued function of the magnetic field strength H, and there is no hysteresis. Hysteresis is the phenomenon that after magnetization of a magnetic material, B will not decrease along the original magnetization curve when H decreases, is no longer a single-valued function of the magnetic field strength H, and the process is related to the magnetization experience previously experienced. In accordance with the MTJ structure described above, which contains a ferromagnetic layer, it is a magnetic material, and the internal defects and anisotropy are difficult to eliminate in the fabrication process, and thus the general phenomenon of hysteresis also exists.

Reducing the effects of hysteresis through fabrication techniques and structural optimization of the magnetoresistive material itself, such as controlling the intrinsic causes of internal anisotropy, usually requires significant time and economic costs.

Closed-loop operation of current sensor modules based on TMR sensing elements enables self-compensation of hysteresis. However, this type of closed-loop operation requires a high degree of uniformity in the wound coil and does not have a good suppression of external disturbances such as crosstalk and changes in the position of the current-carrying conductor. Therefore, in order to realize self-compensation while ensuring the anti-interference capability, based on the principle of equal ampere-turns, the magnetic core, the compensation coil and the signal processing circuit are used to realize the closed-loop operation to compensate the magnetic field at the sensing element.

2.3. Optimized design of multi-stage magnetic loop current sensor

2.3.1. Determination of magnetic property performance evaluation indexes. In order to assess the effectiveness of the new multi-stage magnetic ring structure in terms of its ability to gather magnetism and resistance to external magnetic interference, and to facilitate comparison with the performance of the traditional single magnetic ring structure, the TMR magnetic field measurement sensitivity A and the relative error of magnetic field measurement under the influence of interfering currents MC are defined to characterize the performance of the sensor's induced front-end magnetism in the case of leakage current measurement scenarios oriented to power equipment. To wit:

$$A = \frac{|B_{mrs}|}{|B_{nmrs}|} \tag{11}$$

In Eq. (11), B_{nmrs} is the value of magnetic induction intensity measured by the TMR sensor without magnetic ring structure, and B_{mrs} is the value of magnetic induction intensity measured by the TMR sensor with magnetic ring structure. The larger A indicates the higher sensitivity of the magnetic field measurement at the front end of the TMR sensor. Namely:

$$MC = \frac{|B_{imf} - B_{nimf}|}{|B_{nimf}|} \times 100\% \tag{12}$$

In equation (12), B_{nimf} is the value of magnetic induction intensity measured by the TMR sensor in the absence of interference, B_{imf} is the value of magnetic induction intensity measured by the TMR sensor in the presence of interference, and the smaller the MC is, the higher the accuracy of the magnetic field measured by the TMR.

2.3.2. Optimized design of multi-stage magnetic ring structure:

1) Selection of Optimization Variable Parameters. In this paper, we design a multistage magnetic ring structure with an inner diameter Φ of 20 mm. According to the TMR related chip package model, it is tentatively determined that d =6mm, in order to reduce the production cost and optimize the overall volume of the sensor, it is determined that h =12mm, N=5. Considering the placement size of the TMR module, the thickness of the inner stage polymagnetic layer p needs to be greater than or equal to 6mm.

In order to meet the development trend of miniaturization of sensors and obtain the optimal volume of high-performance three-stage magnetic ring structure, it is finally determined that p and $th_1 - th_2$ of the multi-stage magnetic ring structure are the structural size of the optimization parameters, and the required size optimization problem is converted into a dual-objective optimization synthesis problem with the smallest size and the optimal antimagnetic capability of the TMR.

2) Establishment of objective function. The mathematical model of the dual-objective optimization problem established in this paper is shown in equation (13):

$$\begin{aligned} &\min M = \sum_{j=1}^{4} z_j MC_j(I', p, th_1, th_2) \\ &\min C = p + th_1 + th_2 \\ &st. \begin{cases} p \in [PL, PH] \\ th_1 \in [HL, HH] \\ th_2 \in [TL, TH] \end{cases} \end{aligned} \tag{13}$$

where $MC_f()$ is the true mapping relationship of the magnetic field measurement error due to the j nd angular interference at a certain determined interference intensity. z_j is the weighting of the magnetic field interference at each angle, PL is the minimum value of the thickness of the inner level polymagnetic layer. PH is the maximum value of the thickness of the inner stage poly-magnetic layer, HL is the minimum value of the secondary aluminum layer. HH is the maximum value of the secondary aluminum layer, TL is the minimum value of the tertiary magnet layer, and TH is the maximum value of the tertiary magnet layer.

In this paper, the weighted average method and the entropy weight method are combined to define the weight size, and the combination of the weighted average method and the entropy weight method can include the numerical size and the influence of fluctuation information. The expression of z_j is shown in (14):

$$z_j = a\eta_j + c\omega_j \tag{14}$$

where η_j is the weighted average weight of the j nd perspective. a is the proportion of weighted average weight, ω_j is the entropy weight of the j th angle, c is the proportion of entropy weight.

Keep the center wire through ImA current, change the external interference current for a period of change area, r from lmA-1A, interval value, calculate the size of the relative error of the magnetic field MC, the formation of the matrix V, in order to explore its various angles of the interference current error affect the degree of the situation. That is:

$$V = \begin{bmatrix} v_{11} & v_{12} & \cdots & v_{1n} \\ v_{21} & v_{22} & \cdots & v_{2n} \\ \vdots & \vdots & \vdots & \vdots \\ v_{m1} & v_{m2} & \cdots & v_{mn} \end{bmatrix} \tag{15}$$

where $m = 20, n = 4$.

η_j is calculated according to equation (16):

$$\eta_j = \frac{\sum_{i=1}^{m} v_{ij}}{\sum_{j=1}^{n}\sum_{i=1}^{m} v_{ij}} \tag{16}$$

j fixed, the weight of the i nd sample is calculated as shown in equation (17):

$$p(v_{ij}) = \frac{v_{ij}}{\sum_{i=1}^{m} v_{ij}} \tag{17}$$

Calculate the entropy of the magnetic field error at the j st angular disturbance:

$$e_j = -k\sum_{i=1}^{m} p(v_{ij}) \ln p(v_{ij}) \tag{18}$$

where $k > 0$, and $k = 1/\ln m, 0 \le e_j \le 1$.

For computational convenience, define $G = (g_1, g_2, \ldots, g_n)$, which is proportional to the variability of the indicator measurements, then:

$$g_j = 1 - e_j \tag{19}$$

The entropy weight of the j st interference angle is obtained by normalization:

$$\omega_j = \frac{g_j}{\sum_{j=1}^{n} g_j} \tag{20}$$

As this paper to achieve the goal of the center of gravity facing the angle magnetic field interference, the integrated magnetic field measurement error is minimized, to ensure that the interference impact of the larger angle can still ensure that the TMR to obtain a low magnetic field calculation error.

3) Algorithm optimization process. GWO algorithm, despite its good convergence speed, but in the search for the global optimal solution is still searching for the influence of the path, falling into the local optimum [21]. In order to strengthen the exploration ability of GWO, the GWO algorithm is improved as follows:

(1) Chaotic mapping initialization.

(2) Adaptive descent strategy.

(3) Position update correction.

Combining the above improvement points, the ACGWO-BP algorithm is developed for parameter optimization of BP algorithm.

Multi-stage magnetic ring structure size optimization considered by the sensor measurement anti-interference ability and sensor volume miniaturization dual objectives, the two are interrelated, and need to balance and coordinate to ensure that each objective to achieve the optimal effect, in order to adapt to the actual needs of the project, so this paper selects the non-dominated sorting genetic algorithm (NSGA-II) on the multi-stage size structure for multi-objective optimization. Finally, this paper builds the ACGWO-BP-NSGA-II optimization design framework. Firstly, initialize the relevant parameters such as the number of populations NN, dimensions D, and iterations G. Produce the initial population Pt, calculate the individual fitness of population Pt, followed by an iterative session. Produce new offspring population Qt through crossover, mutation and selection, splice Qt

with Pt to form a new population Rt. In the iterative process, compute the target value and perform non-dominated sorting on the new population Rt, and sort the population members of Rt to different frontiers according to the non-dominated rank. Subsequently, the appropriate nn individuals are selected as the new population $Pt+1$ until the number of iterations is complete. Finally, the population that results from the last iteration will be selected as the best individual population output.

3. TMR current sensor based energy meter design

3.1. Energy Meter Hardware Design Program

Considering the need to design the peripheral conditioning circuit for the TMR current sensor to solve the problem of matching the output signal of the current sensor with the input signal range of the metering chip. In addition, the use of "special power metering chip + main control chip" has become the mainstream design ideas for research and development of power meters. In this paper, the power meter is designed with the RN8209C metering chip of Rui Neng Micro and the R7F0C004 power meter special master control chip of Renesas. These two chips have a higher degree of integration, which reduces the design task of other external circuits of the chip and allows people to invest more energy in solving the application problems of TMR current sensors.

The design and testing of the power meter in this paper follows GB/T 17215.211-2017 and other relevant technical standards.

The TMR current sensor-based single-phase power meter in this paper is also designed according to the standard of level 2 meter, and the specifications and technical parameters of the specific design are shown in Table 1.

Table 1. The specification and technical parameters of the energy meter

Accuracy rating	Rated frequency	Rated voltage	Power working voltage	Current	Impulse constant (imp/kWh)
2	55 Hz ± 6%	220 V	0 Un ~1.23 Un	5(60) A	1200

The environmental conditions of the work are shown in Table 2.

Table 2. Environmental condition

Reference temperature	Standard working temperature	Relative humidity	Atmospheric pressure	Limit working temperature and storage and transportation temperature
25℃	-26℃~65℃	<96%	65 kPa ~110 kPa	-42℃~70℃((4000 meters above sea level))

The functional requirements are shown in Table 3.

Table 3. Functional requirement

Function	Describe
Electric metering	The measurement and storage of total electricity.
Clock	With a built-in clock with a warm complement, the temperature range of the temperature range of the -25~60℃ is less than 1s/d.
Data storage	Data on 12 settlement days can be stored.
Event record	The energy meter can record the time and end of the recent 10 events.
Communication	Rs485ir and infrared 2 communication, communication channel physical layer independence.
Display	There are key display and automatic display, which can display information such as electricity, voltage, current, power and time.
Load record	Record the information of the energy meter. Can store the interval of 1 minute and not much in 12 days.

The energy meter adopts the design scheme of special metering chip combined with the main control chip, and the system structure of single-phase energy meter based on TMR current sensor is shown in Fig. 2.

In this paper, the power meter requires a voltage of 5V, -5V and 2.5V. 5V is used to supply power to the metering chip, the main control chip and other circuits, and ±5V and 2.5V are used to supply power to the amplifiers of the peripheral conditioning circuits of the TMR current sensor.

The metering chip selected for the metering module is RuiNeng Micro RN8209C, which collects voltage signals with a voltage divider resistor and current signals with a TMR current sensor, and the metering chip realizes the calculation of various data.

MCU module is the control center of the whole meter system. The main control chip is R7FC004 from Renesas, which has a relatively high degree of integration and comes with a crystal, LCD driver circuit and RTC clock circuit, which reduces the complexity of the system circuit design and is suitable for power meter design.

The storage module mainly completes the functions of real-time data recording, safe data storage, and ensuring that the data is not lost in power-down, and adopts the IIC synchronous communication mode.

The communication module includes RS485 communication and infrared communication to realize the data transmission between the master station and the meter.

Universal Asynchronous Transceiver Transmitter UART, a universal serial data bus, the communication process follows the principle of sending the low bit first and then sending the high bit, used for asynchronous communication.

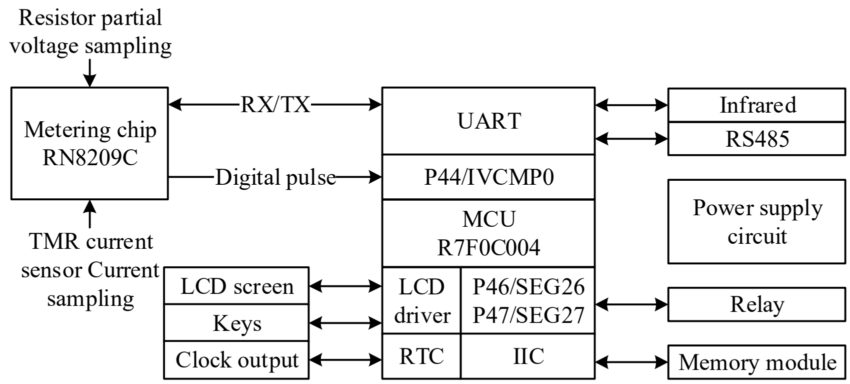

Fig. 2. Mono-phase energy meter system structure based on TMR current sensor

3.2. MCU Control Circuit and Other Circuits

R7F0C004 is a special MCU chip for power meter, which is a 16-bit microcontroller with low power consumption and high performance. The chip has a built-in LCD controller/driver, RTC clock, multiple communication ports, low voltage detection circuit and other practical peripherals, the chip also has a high-precision (±1%) oscillator and 24MHz CPU, widely used in a variety of energy meter design, and the subsequent products are constantly being updated and upgraded. The chip greatly simplifies the software and hardware design of the energy meter and reduces the production cost.

The single-phase power meter based on TMR current sensor designed in this paper has two sets of system clocks, one main and the other secondary. The main system clock is used during normal operation of the energy meter. When power down, the system enters the low-power mode and uses the vice system clock. After powering up again, it switches to the main system clock and the energy meter enters the normal operating mode.

3.3. Metering and Conditioning Circuitry

The metering circuit is mainly composed of current sampling circuit, voltage sampling circuit and peripheral circuit of metering chip. In this paper, the design of the power meter selected by the metering chip model RuiNeng micro RN8209C.

TMR current sensor output voltage is 2.5V ± 625mV pulsating DC voltage output. And the current channel input pin of the power metering chip RN8209C has a maximum input Vpp of ±1000mV for normal operation. This section proposes to realize the regulation of the output signal of TMR current sensor, firstly, after the subtraction circuit filters out the DC voltage of 2.5V, so that the output signal of TMR current sensor becomes a sinusoidal signal with the amplitude of ±625mV, and then, after the divider circuit controls the amplitude at ±100mV, and finally, the output is outputted by the noise reduction and antialiasing circuit to the input of the current signal of the RN8209C metering chip. The subtraction circuit is used to filter out the 2.5V DC voltage in the output voltage signal of the TMR current sensor.

The single-phase energy meter designed in this paper uses resistance voltage divider for voltage sampling. In the resistance divider network with resistors and capacitors to form a filter circuit, the same can be achieved to weaken the role of high-frequency interference, and the cost is lower.

3.4. *Specific design of current monitoring module*

3.4.1. Signal Acquisition Module Design. The signal acquisition module focuses on the amplification of micro-current signals and contains a preamplifier circuit, a secondary signal amplifier circuit, and a second-order low-pass filter circuit. In this paper, ADI's high-speed instrumentation amplifier AD8421 is used instead of a three-operation amplifier circuit.AD8421 has a bandwidth of 10MHz, a slew rate of 35V/μs, and a build-up time of 0.01% (G=1) of 0.7μs can be realized to amplify high-frequency signals. The reliability of this performance is guaranteed even at high gain.

The AD8421 is rated for operation from -40°C to +85° C. The internal structure of the chip is an integrated triple op-amp circuit that requires very few peripheral devices, and the amplification range can be controlled by connecting a variable resistor externally between pins 2 and 3. The circuit uses potentiometer R_{32} to realize the adjustable gain and the expression for the gain G is shown in equation (21):

$$G = 1 + \frac{9.9}{R_{32}} \tag{21}$$

In order to ensure the accuracy of the signal and reduce the number of times the deviation, the amplification of the pre-stage circuit should not be set too large, so the signal needs to be amplified again, so add the secondary amplifier circuit. Operational amplifier chip using ADI company's AD847.

The gain of the second-order Butterworth low-pass filter is:

$$G^2(\omega) = \left|H(j\omega)\right|^2 = \frac{G_0^2}{1 + \left(\frac{\omega}{\omega_c}\right)^4} \tag{22}$$

where ω_c is the cutoff frequency and G_0 is the DC gain, which can be seen to be suppressed when $\omega > \omega_c$.

According to the principle of false short and false short at the operational amplifier, it can be deduced that the transfer function of Butterworth is:

$$A_v(s) = \frac{V_{oUT3}(s)}{V_{oUT2}(s)} = \frac{1 + \frac{R_{30}}{R_{34}}}{1 + \left(2 - \frac{R_{30}}{R_{34}}\right) C_{34} R_{36} s + \left(C_{34} R_{36} s\right)^2} \tag{23}$$

The transfer function of the second order Butterworth filter circuit is:

$$A_v(s) = \frac{A_0}{\frac{s^2}{\omega^2} + \sqrt{2}\,\frac{s}{\omega_c} + 1} \tag{24}$$

According to the characteristics of the TMR sensor, the bandwidth of the sensor can be up to 500 Hz, and if the bandwidth of the Butterworth filter circuit is set to 1 MHz, the combination of the two equations can be deduced:

$$A_0 = 1 + \frac{R_{30}}{R_{34}}, \frac{\sqrt{2}}{\omega_c} = \left(2 - \frac{R_{30}}{R_{34}}\right) C_{34} R_{36} \ldots, \frac{1}{\omega_c} = C_{34} R_{36} \ldots, \omega_c = 2\pi \cdot 1MH_z \tag{25}$$

Take $C_{34} = C_{39} = 0.1\mu F$, then $R_{36} = R_{37} = 4k\Omega$, $R_{34} / R_{30} = 0.59$, and choose the appropriate resistor size as $R_{30} = 100k\Omega$, $R_{34} = 60k\Omega$.

3.4.2. Bias Regulation and Temperature Compensation Module. The best use is achieved when the source impedance of the REF pin of the AD8421 should be kept below $1\,\Omega$. The voltage following circuit is constructed using the op-amp AD847, and its in-phase input is divided in series using the adjustable resistor R39 and a high-precision resistor R41 to achieve the purpose of voltage regulation.

The next step is to design a compensation circuit for the influence of temperature factor on the output result. The compensation method is mainly to use a power supply that can change the voltage level with the temperature change to supply power to the TMR2905, and the specific voltage relationship is as follows.

$$V_1 = \left(1 + \frac{R_{38}}{R_{40}}\right) \times 5 \tag{26}$$

R_{40} is a temperature-sensitive resistor that decreases in resistance as the temperature rises. As the temperature rises, the resistance decreases accordingly, and the supply voltage rises.

3.4.3. Communication module design. In order to realize the transmission of the collected signals, it is necessary to add a communication module, and this device uses a 4G module to transmit the signals.The 4G module adopts the E29V-G model produced by Tashi Internet of Things, the interface type is TTL serial port, the size is 40mm×40mm×15 mm, the working current is 0.2 A, the working voltage is 12V, it supports the TCP/IP protocol, and the transmission rate is 120kbps, support SMS function.

After the device collects the signal, it needs to be transmitted to the platform through the 4G module, and the platform used in this research is the T-LINK platform, which can realize the real-time display of the collected signal and waveforms, support the storage and download of data, and can retain historical data.

3.4.4. Circuit protection module design. The circuit protection module consists of two relays, through the breakdown voltage of the semiconductor device and the principle of circuit voltage divider to control the on-off of the relay, so as to complete the judgment of the size of the signal, to realize the protection of the circuit, to prevent the circuit from overloading and burning.

The circuit protection module of this device is to judge the size of the V+ and V- models respectively, and there is a transistor installed in each way, and the conduction voltage of the transistor is 0.7 V. According to the principle of voltage dividing, when the input voltage exceeds 1.4 V, the semiconductor device will conduct, the relay will start to work, and the whole circuit will be disconnected. No amount of normal leakage current will cause the device to restart, and if an inrush discharge occurs, the device will automatically cut off the power to provide protection.

4. TMR current sensor based system detection

4.1. Sensor performance parameters

The performance of the prototype fluxgate sensor array current measurement was tested using the built test rig. Place the wire under test on the center of the sensor array, trying to ensure that the wire is perpendicular to the PCB board with no bends. There are no other interfering currents around the sensor, away from other ferromagnetic materials.

Two types of copper wires under test were used for the experiment. One is a single-stranded wire with a length of 2.2 m, a circular cross-section, a diameter of 2 mm, and an insulating skin. The other is a multi-stranded copper core wire, 2.2 m long, 2 mm in diameter, with insulating skin. The copper wire is connected to the current source, the measured current is set, the recording function is enabled in the LabVIEW front panel, the sampling frequency is set to 1k, and the measured value is recorded for at least 15 s. The output of the sensor is shown in Fig. 3 when the measured current is 0A.

Due to the influence of geomagnetism, the voltage output of the eight sensors is between 3.36 V and 2.69 V. At this time, the sensors are roughly in the position of the angle of 10° with the meridian and perpendicular to the horizontal plane. The sensor array plane was rotated, and when the plane was at an angle of 45° to the meridian, the sensor voltage output gap was significantly reduced, and the rotation of the sensor array plane was continued. The gap is again maximized at approximately 95° from the meridian, showing that measurements with a single magnetic sensor cannot ignore and eliminate the effects of geomagnetism.

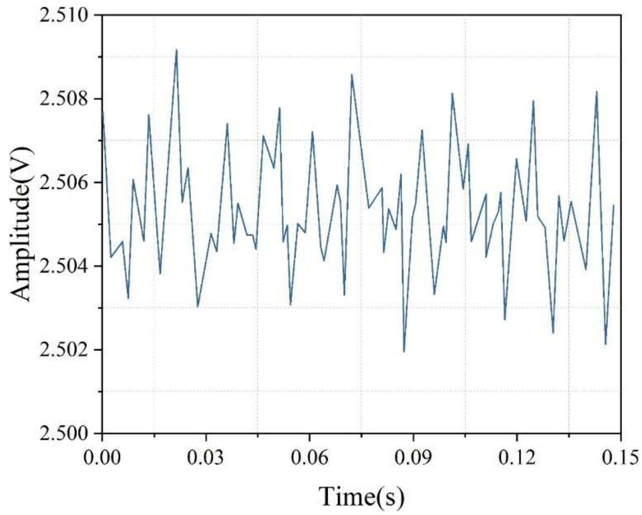

Fig. 3. The voltage output of the sensor voltage is affected by geomagnetic influence

The average value of the sensor output voltage is stabilized at 2.5047V, with positive and negative errors within 0.0015V, which is a certain gap with the ideal output voltage of 2.5V, due to the existence of installation errors, noise, out-of-phase voltage and power supply voltage fluctuations and other factors interfere. In order to try to eliminate this error, the data records can be imported into MATLAB for processing, the voltage output value in different cases and zero current output value to do the difference, the increment is the measured value in different cases. The measured values when the measured current is 1A and 5A, respectively, compared to the results when measuring large currents are more stable, which is due to the weak spatial magnetic field generated by the wire at small currents, and it is difficult to ignore the influence of stray fields.

The linearity test of the sensor was performed by setting the measured current to increase from 0 A to 5A in steps of 0.5 A. The test results were linearly fitted and compared to the expected sensor output. The results of the sensor linearity test are shown in Fig. 4, where Figs. (a) and (b) show the linear fit of the average voltage output of the fluxgate sensor, and the absolute error between the measured and theoretical voltage output of the fluxgate sensor, respectively.

As the measured current increases, the error compared to the ideal sensor output increases, which is related to the experimental environment, installation errors, and at a measured current of 5A, this error will increase by 0.15%. If 5A is used as the full scale state, then the linearity of the sensor $\gamma L = \pm 0.3\%$. The theoretical output sensitivity of the sensor is 1.2214mV/A, and the actual measurement sensitivity is about 2.051mV/A.

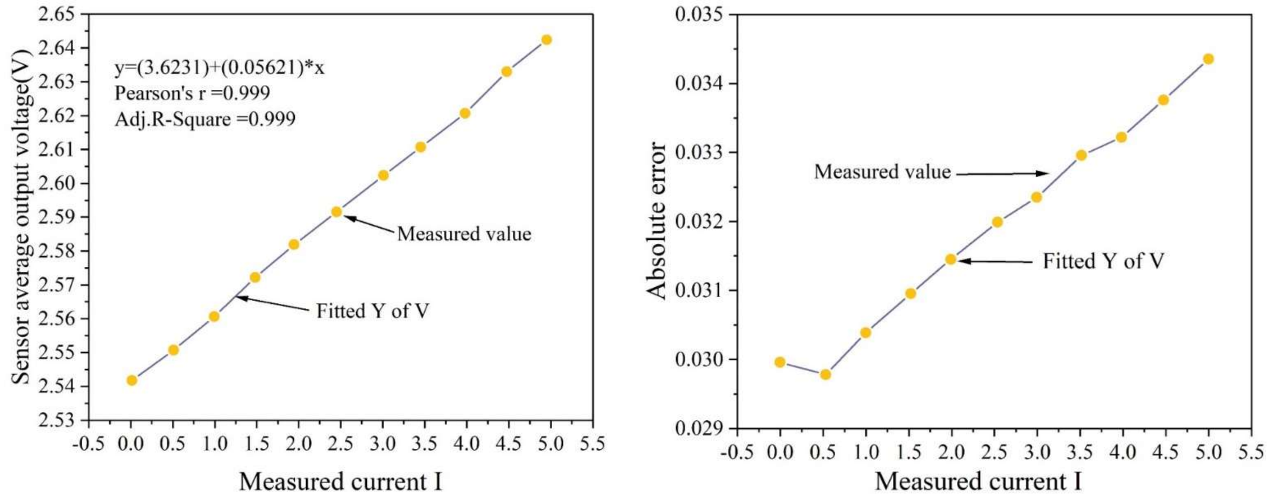

(a) Mean voltage output linear fitting (b) Absolute error

Fig. 4. Sensor linear test results

4.2. TMR measurement system commissioning and calibration

In this chapter, DC current and AC current tests are carried out sequentially using the designed TMR sensor measurement device.

4.2.1. DC current test. In the DC current test, a 7.2V NiCd battery was used as the current source, and the NiCd battery was connected in series with resistors of different resistance values to form a loop in order to generate current. In the DC current test, the distance between the TMR sensor and the current is varied, the loop current value and the sensor output voltage before and after energization are measured, and the relative error of the measurement result is calculated according to the equation of output voltage versus current. The loop current value is obtained by dividing the series resistance by the voltage of the current source, and the sensor output voltage before and after energization is measured directly with a voltmeter.

When the distance of the TMR sensor from the current is 1.8mm, the series resistance is changed to obtain different sizes of current, and the polarity of the current source is changed to obtain forward and reverse currents, and the test results are shown in Table 4. The maximum measured current under both forward and reverse measurements does not exceed 6A.

Table 4. Experimental results of the chip and conductor spacing 1.8 mm

	Measured current (A)	No magnetic field voltage (mV)	The voltage of a magnetic field (mV)	Voltage difference (mV)	Measured current/voltage difference	Theoretical current (A)
Forward measurement	0.65	19.3	22.4	4.5	163.58	0.63
	1.37	18.6	27.5	8.2	150.21	1.39
	5.42	18.1	50.6	32.4	166.37	5.04
Reverse measurement	0.69	21.4	23.1	4.3	161.42	0.62
	1.21	22.3	32.6	8.9	152.01	1.41
	5.06	23.4	52.7	31.5	163.28	4.93

In the DC current test, single-ended input amplification is used for output voltage processing, and the obtained current and voltage difference follow the following equation:

$$I = \frac{4\pi d\Delta U}{k\left(cos\theta_1 - cos\theta_2\right)} \tag{27}$$

where, $k = 5mv/Oe$, d is the distance between the TMR sensor and the wire. ΔU is the absolute value of the difference between the voltage with magnetic field and the voltage without magnetic field. θ_1 and θ_2 are the angles between the TMR sensor and the beginning and end of the wire, which can be regarded as infinitely long with respect to the TMR sensor, θ_1=0°, θ_2=180°, respectively.

The theoretical current value I_{theo} can be calculated from the above equation and the measured voltage difference, and the relative error δ is calculated from the measured actual current value I_{real} and the calculated theoretical current value with the following formula:

$$\delta = \frac{\left|I_{real} - I_{theo}\right|}{I_{real}} \times 100\% \tag{28}$$

The relative errors of the theoretical current values calculated from the measurement experiments are shown in Table 5, with ΔU_1=5.2 mV, I_1=706.6 mA, and the relative error δ_1=0.013% in the forward measurement experiments.

Through the above error analysis, it can be seen that the relative error between the actual current value measured experimentally and the theoretical current value deduced by the formula is within 5%. And there is no significant difference in the relative error between the forward current test results and the reverse current test results, from which it can be inferred that the current flow direction has no effect on the measurement results of the TMR measurement system.

Table 5. The relative error of the theoretical current value

Measuring experiment	ΔU (mV)	I (mA)	δ
Forward measurement experiment	ΔU_1=5.2	I_1=706.6	δ_1=0.013
	ΔU_2=7.6	I_2=1.55	δ_2=2.34
	ΔU_3=33.7	I_3=5.12	δ_3=1.86
Reverse measurement experiment	ΔU_4=4.5	I_4=693.4	δ_4=0.02
	ΔU_5=8.7	I_5=3.3	δ_5=3.25
	ΔU_6=33.4	I_6=33.6	δ_6=4.76

4.2.2. AC current test. The AC current test set consists of a voltage regulator, a transformer, a series resistor and a wire. By adjusting the output voltage of the regulator, the output voltage of the op-amp module is measured under different conditions such as 3A peak current, respectively. Select the measurement results under 3.0A and 90mA current peaks to draw waveforms, and the current-voltage waveforms in the industrial frequency alternating current test are shown in Figure 5. The yellow waveform corresponds to the loop current measured by the current clamp, and the blue waveform corresponds to the output voltage of the op-amp module.

From the waveform results in the figure, it can be clearly observed that the trend of the output voltage waveform is consistent with the trend of the current waveform, which indicates that the TMR sensor is able to sense the magnetic field generated by the current.

As can be seen from Figure (b), when the current peak value is as small as 90mA, due to the limitations of the oscilloscope range, accuracy and the existence of voltage fluctuations in the channel itself, the noise in the voltage waveform is obvious, so 90mA is the smallest current peak value that can be accurately measured in the current test. At this time, the current is always kept in the range of [-0.2,0.2], and the output voltage is in the range of [-0.1,0.1].

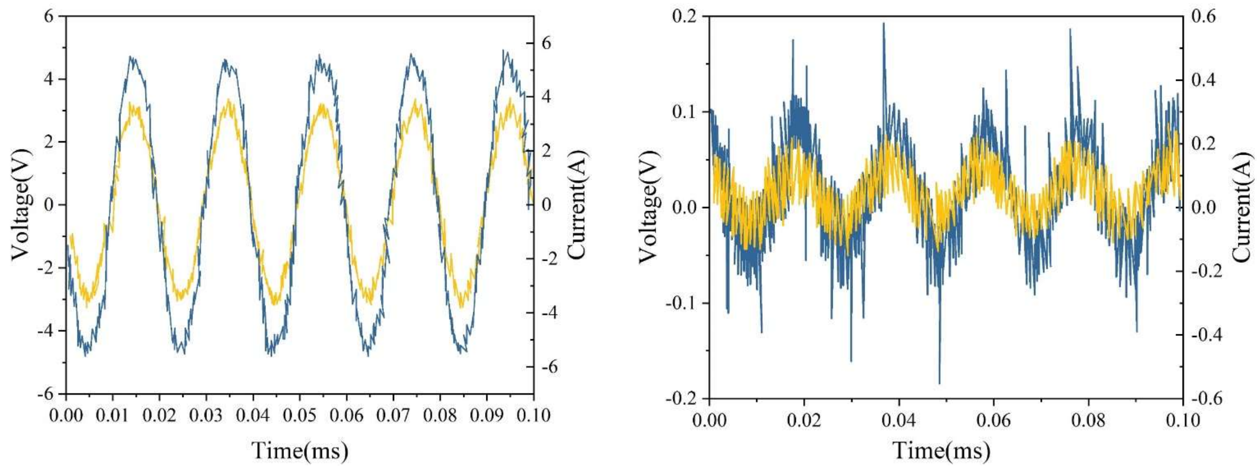

(a) 3.0A peak current (b) 90A peak current

Fig. 5. Industrial frequency alternating current test

In order to determine whether the TMR sensor can accurately measure the current, the change in the output voltage of the op-amp module when the current is 0 and the output voltage under the peak current is recorded as the voltage difference, and the ratio of the peak current to the voltage difference is calculated to see whether the ratio is the same for each set of data. The peak current relative error results are shown in Table 6.

In different peak current tests, the ratio of the peak current I_p to the voltage difference ΔU can be regarded as constant in a small range, so the black-box model can be fitted to the unitary function equation of the two. When the output voltage of the op amp module is small to a certain value, the clutter interference and human readings existing in the oscilloscope measurement channel itself will cause a large error in the measurement results. In order to minimize the impact of the error of the above factors, take the first four groups of larger test data to participate in the function fitting, the fitting of the theoretical peak current I_p and the voltage difference ΔU relationship between the equation is as follows:

$$I_p = 0.7251\Delta U - 0.003 \tag{29}$$

Thus, the relative error of each set of test data can be derived. As can be seen from the results in the table, the relative errors between the theoretical peak current and the actual peak current measured by the current clamp are all within 5%. Considering the presence of system clutter signals and the errors introduced by the readings, the relative error of 5% is within the acceptable range. The theoretical peak current calculated from the measured voltage difference and the fitted equation has credibility. The results of this AC current test fully demonstrate that the TMR sensor is capable of AC current measurement.

Table 6. Relative error of peak current

Peak current (A)	Voltage difference (V)	$I_p / \Delta U$	Theoretical peak current (A)	Relative error(%)
3.42	4.23	0.71	3.462	1.63
2.71	4.20	0.66	2.813	1.77
2.51	3.62	0.72	2.425	0.35
2.03	2.89	0.74	2.041	3.64
1.89	2.32	0.69	1.983	3.32
1.42	1.39	0.63	1.635	0.25

1.31	1.57	0.51	1.414	3.96
0.78	0.81	0.73	1.121	4.51
0.73	0.56	0.74	0.854	3.72
0.55	0.55	0.76	0.736	0.23
0.41	0.34	0.77	0.524	0.89
0.30	0.27	0.63	0.331	1.86
0.19	0.14	0.66	0.186	2.31

4.3. Current measurement module performance index test

4.3.1. Accuracy measurements. In order to assess the accuracy of the measurement data of the current meter, different micro-current signals are tested with a time interval of 3s and 300 consecutive measurements, and the average of the short-term measurement data is taken as the measurement result of the instrument. Comparison and analysis with the multifunction multimeter measurement results and calculate the relative error, accuracy measurement results shown in Table 7.

The relative errors of the current measuring instruments designed in this paper are less than 10% in the whole range, while the relative errors in the range are generally about 6%. The relative error of 3 nA is the smallest, with a value of -0.31%. 30 pA has the largest relative error, with a value of 6.04%.

Table 7. Accuracy measurement results

Gear	Theoretical input	I_{IN} value (A)	V_{OUT} Theoretical value(V)	V_{OUT} Measured value(V)	Relative error (%)
0	No load			0.0525	
1	1.7 pA	1.94×10^{-12}	1.94	0.2166	3.65
2	30 pA	2.61×10^{-11}	2.61	2.2259	6.04
3	300 pA	1.993×10^{-10}	1.993	0.2136	-1.56
4	3 nA	1.9986×10^{-9}	1.9986	2.3445	-0.31
5	30 nA	2.0061×10^{-8}	2.0061	0.2021	0.48
6	300 nA	1.9345×10^{-7}	1.9345	2.0475	5.65
7	3 μA	2.0113×10^{-6}	2.0113	2.2103	5.33

4.3.2. Precision measurements. Repeated measurements are performed on the same signal to evaluate the precision of the instrument. The microcurrent signals with output currents of 30 pA, 3 nA, and 3 μA from the signal source are measured with the designed instrument to evaluate the precision of class pA, nA, and μA measurements. Ten sets of data are measured and each set of measurement results is the average of the 10 data, the data are recorded and the relative standard deviation RSD is calculated. The average value of 10 groups of data is also sought, and the relative standard deviation of 10 groups of data is calculated. The results of the precision measurements are shown in Fig. 6, where Figs. (a), (b), and (c) are the measurements for the given currents of 30 pA, 3 nA, and 3 μA, respectively.

The current meter designed in this paper has less data fluctuation in level pA, nA and μA measurements, i.e., the precision of the instrument is high. 30 pA, 3 nA, 3 μA measurements of the relative standard deviation of the data do not exceed 0.144%, 0.035%, 0.129%. The largest relative standard deviation in the data for measurement 3 μA is only 0.0284%.

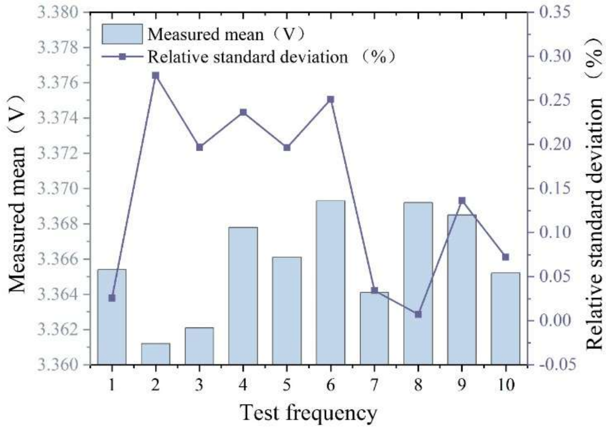

(a) 30 pA

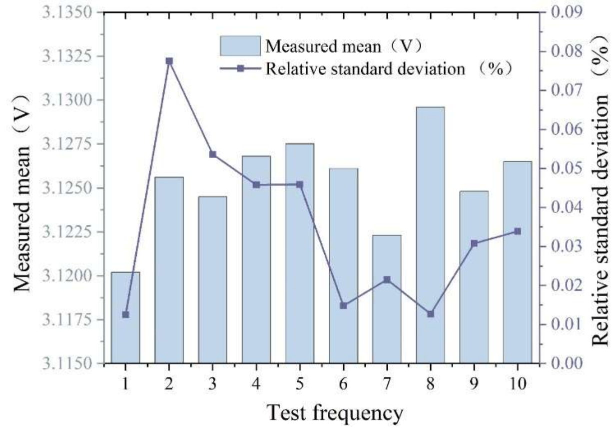

(b) 3 nA

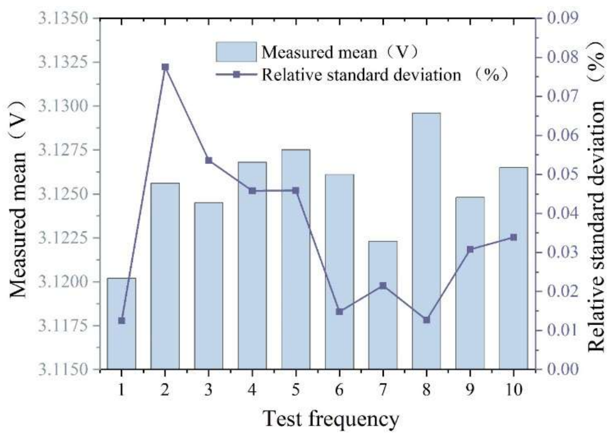

(c) 3 μA

Fig. 6. Precision measurement results

4.3.3. Linearity assessment. For the actual output value of the instrument V_{OUT} and the micro-current detector to be measured between the current value I_{IN} of the assessment process for, the use of micro-current instrument on the signal source generated by a certain gradient change in the micro-current signal to start the measurement of the results of the I_{IN} average value of the X-axis and the measurement of the V_{OUT} average value of the Y-axis to be made and its linear fitting, and at the same time calculate the curve of the linear correlation coefficient.

As the microcurrent meter designed in this paper has a wide measurement range (i.e., more than 6 orders of magnitude), so the entire measurement range is divided into 4 groups of ranges to carry out measurements, the measurement range of 4, 3, 2, 1, respectively, corresponding to the microcurrent detection module in the feedback resistance value of 100 $G\Omega$, 1 $G\Omega$, 10 $M\Omega$ and 1 $M\Omega$.

The microcurrent meter is used to measure each group of input current values that change according to a certain gradient I_{IN}, and the measurement results V_{OUT}, where each gradient of the measured value will be averaged over 100 consecutive measurements with a time interval of 3s. The linearity measurements at different ranges are shown in Table 8.

The different ranges are 21.3, 997.1, 99.758, 2.4931, 2.3621, 1.0236, 1.0645, and 0.2687 for different ranges at the fifth test with signal source gears of 1, 3, 5, 5, and I_{IN} vs. V_{OUT}, respectively.

Table 8. Linear measurement results under different ranges

Test number	Source gear	$I_{IN}(pA)$	$V_{OUT}(V)$
1	Range 4, R_F =100 $G\Omega$,gear=1	0.0	0.0518
	Range 3, R_F =1 $G\Omega$,gear=2	53.2	0.0604
	Range 2, R_F =10 $M\Omega$,gear=4	6.638	0.0463
	Range 1, R_F =1 $M\Omega$,gear=5	0.5214	0.0596
2	Range 4, R_F =100 $G\Omega$,gear=1	5.6	0.6243
	Range 3, R_F =1 $G\Omega$,gear=2	100.7	0.1124
	Range 2, R_F =10 $M\Omega$,gear=4	12.396	0.1257
	Range 1, R_F =1 $M\Omega$,gear=5	1.0521	0.1396
3	Range 4, R_F =100 $G\Omega$,gear=1	12.3	1.2531
	Range 3, R_F =1 $G\Omega$,gear=2	203.4	0.3266
	Range 2, R_F =10 $M\Omega$,gear=4	22.126	0.2355
	Range 1, R_F =1 $M\Omega$,gear=5	1.5237	0.1868
4	Range 4, R_F =100 $G\Omega$,gear=1	16.5	1.7251
	Range 3, R_F =1 $G\Omega$,gear=3	500.4	0.5274
	Range 2, R_F =10 $M\Omega$,gear=5	51.742	0.5398
	Range 1, R_F =1 $M\Omega$,gear=5	1.9934	0.2342
5	Range 4, R_F =100 $G\Omega$,gear=1	21.3	2.3621
	Range 3, R_F =1 $G\Omega$,gear=3	997.1	1.0236
	Range 2, R_F =10 $M\Omega$,gear=5	99.758	1.0645
	Range 1, R_F =1 $M\Omega$,gear=5	2.4931	0.2687

5. Conclusion

In this paper, the TMR sensor is used to establish the current measurement module and design the power meter containing the TMR current sensor. Optimize the design of multi-stage magnetic loop current sensor, optimize the variable parameters and improve the GWO algorithm, and propose the ACGWO-BP algorithm. Test the sensor performance and analyze the performance of the current measurement module.

1) The performance of the current measurement module of the fluxgate sensor array is tested, and the sensor output curve is obtained when the measured current is 0A at a sampling frequency of 1000. The linearity of the sensor is tested, and as the measured current increases, the error compared to the ideal sensor output increases, which is related to the experimental environment. The linearity γL of the sensor is about $\pm 0.3\%$ when the sensor 5A is at full scale.

2) In the DC current test, a 7.2V nickel-chromium battery was used as the current source, and the relative error between the actual current value of the experiment and the theoretical current value deduced by the formula was within 5%. In the AC current test, 90mA was derived from the voltage waveform distribution as the minimum peak current value that could be accurately measured in the test. The relative error between the theoretical peak current value and the actual peak current value measured by the current clamp is within 5%. Thus, the measurement module of the TMR current sensor designed in this paper has the credibility of the voltage difference between the DC current test and the AC current test.

3) In order to further test the performance of the current measurement module, the accuracy, precision and linearity indexes are evaluated respectively, and the relative standard deviations of the measurement data at level 30 pA, level 3 nA and level 3 μA do not exceed 0.144%, 0.035% and 0.129%. The current meter designed in this paper has less data fluctuation in level pA, nA and μA measurements, which means that the precision of the instrument is high.

Acknowledgements

This work was supported by State Grid Corporation Technology Project (5700-202219210A-1-1-ZN).

References

[1] Nwagbo, C. L., & Baah, B. (2022). A comparative study of basic types of energy meters and metering. Global Journal of Engineering and Technology Advances, 10(1), 117-124.

[2] Masnicki, R. (2018, June). Some remarks on the accuracy of energy meters. In 2018 IEEE International Conference on Environment and Electrical Engineering and 2018 IEEE Industrial and Commercial Power Systems Europe (EEEIC/I&CPS Europe) (pp. 1-5). IEEE.

[3] Zhou, K., Yang, C., & Shen, J. (2017). Discovering residential electricity consumption patterns through smart-meter data mining: A case study from China. Utilities Policy, 44, 73-84.

[4] Avancini, D. B., Rodrigues, J. J., Martins, S. G., Rabêlo, R. A., Al-Muhtadi, J., & Solic, P. (2019). Energy meters evolution in smart grids: A review. Journal of cleaner production, 217, 702-715.

[5] Morello, R., De Capua, C., Fulco, G., & Mukhopadhyay, S. C. (2017). A smart power meter to monitor energy flow in smart grids: The role of advanced sensing and IoT in the electric grid of the future. IEEE Sensors Journal, 17(23), 7828-7837.

[6] Pitì, A., Verticale, G., Rottondi, C., Capone, A., & Lo Schiavo, L. (2017). The role of smart meters in enabling real-time energy services for households: The Italian case. Energies, 10(2), 199.

[7] Michalec, Ł., Jasiński, M., Sikorski, T., Leonowicz, Z., Jasiński, Ł., & Suresh, V. (2021). Impact of harmonic currents of nonlinear loads on power quality of a low voltage network–review and case study. Energies, 14(12), 3665.

[8] Pereira, J. L. M., Leal, A. F. R., Almeida, G. O. D., & Tostes, M. E. D. L. (2021). Harmonic effects due to the high penetration of photovoltaic generation into a distribution system. Energies, 14(13), 4021.

[9] Diahovchenko, I., Volokhin, V., Kurochkina, V., Špes, M., & Kosterec, M. (2019). Effect of harmonic distortion on electric energy meters of different metrological principles. Frontiers in Energy, 13, 377-385.

[10] Gbadamosi, S. L., Nwulu, N. I., & Siano, P. (2022). Harmonics constrained approach to composite power system expansion planning with large-scale renewable energy sources. Energies, 15(11), 4070.

[11] Qi, C., Liu, Y., Wang, Y., Bi, C., & Li, W. (2025). Research on Performance Optimization of Agricultural Intelligent Energy Meters Driven by Intelligent Sensors under Overload Conditions. Measurement: Sensors, 101812.

[12] Li, Q., Feng, B., Ma, H., Zhang, Z., Ma, X., & Wang, Y. (2020, April). Big Data Analysis of Intelligent Electric Meters' Faults. In 2020 International Conference on Computer Information and Big Data Applications (CIBDA) (pp. 8-10). IEEE.

[13] Besada, P., Ghali, H. A., & Memon, S. (2022, June). Investigating an influence of temperature and relative humidity on the electrical performance of lithium polymer ion battery using constant-current and constant voltage protocol at small scale for electric vehicles. In The 11th International Conference on Power Electronics, Machines and Drives. Institute of Engineering and Technology (IET).

[14] Apse-Apsitis, P., Vitols, K., Grinfogels, E., Senfelds, A., & Avotins, A. (2018). Electricity meter sensitivity and precision measurements and research on influencing factors for the meter measurements. IEEE Electromagnetic Compatibility Magazine, 7(2), 48-52.

[15] Diahovchenko, I. M., & Olsen, R. G. (2020). Electromagnetic compatibility and protection of electric energy meters from strong magnetic fields. Electric Power Systems Research, 186, 106400.

[16] Li, H. (2024). Analysis of Influence of Wiring Error on Electric Energy Metering Device and Preventive Measures. Journal of Advances in Engineering and Technology, 1(1), 52-62.

[17] Chang, S., Liu, N., Xu, H., Feng, L., Shi, T., Zeng, M., & Hu, J. (2024, March). Analysis of metering misalignment caused by abnormal current of smart energy meter. In 2024 IEEE 7th Advanced Information Technology, Electronic and Automation Control Conference (IAEAC) (Vol. 7, pp. 308-312). IEEE.

[18] Bartolomei, L., Cavaliere, D., Mingotti, A., Peretto, L., & Tinarelli, R. (2020). Testing of electrical energy meters subject to realistic distorted voltages and currents. Energies, 13(8), 2023.

[19] Hirokuni Oda,Seiji Kumagai,Kosuke Fujiwara,Hitoshi Matsuzaki,Hiroshi Wagatsuma,Mikihiko Oogane... & Akihiro Tanimoto. (2024). Advancement in scanning magnetic microscopy utilizing high-sensitivity room-temperature TMR sensors for geological applications. Earth, Planets and Space(1), 169-169.

[20] Bo Wang,San Zhang,Jie Wang,Liqin Jing & Feilong Mao. (2024). A Novel Magnetic Flux Leakage Method Incorporating TMR Sensors for Detecting Zinc Dross Defects on the Surface of Hot-Dip Galvanized Sheets. Magnetochemistry(12),101-101.

[21] Pengjia Yan. (2024). Research on Stock Price Prediction based on the GWO-LSTM-ATT Model. Frontiers in Computing and Intelligent Systems(3),107-114.